

Article

Fe₃O₄-ZnO:V Nanocomposites with Modulable Properties as Magnetic Recoverable Photocatalysts

Ana Varadi ^{1,2}, Cristian Leostean ^{1,*}, Maria Stefan ¹, Adriana Popa ¹, Dana Toloman ¹, Stela Pruneanu ¹,
Septimiu Tripon ¹ and Sergiu Macavei ¹

¹ National Institute for R&D of Isotopic and Molecular Technologies, 67-103 Donat St., 400293 Cluj-Napoca, Romania; ana.varadi@itim-cj.ro (A.V.); maria.stefan@itim-cj.ro (M.S.); stela.pruneanu@itim-cj.ro (S.P.)

² Doctoral School of Chemistry, Babes-Bolyai University, 400028 Cluj-Napoca, Romania

* Correspondence: cristian.leostean@itim-cj.ro; Tel.: +40-264-584037; Fax: +40-264-420042

Abstract: Since semiconductor-based photocatalysis uses solar energy as a free and sustainable energy source and inoffensive photocatalysts, it has been found to be a promising green approach to eliminating dyes, antibiotics, and other pharmaceuticals from water that has been contaminated. In this study, a distinctive magnetic separable Fe₃O₄-ZnO:V photocatalyst is reported. ZnO:V semiconductors have been produced by seed-assisted growth over preformed magnetite to develop Fe₃O₄-ZnO:V nanocomposites. The results indicated nanocomposites with the structure of Fe₃O₄, ZnO:V, according to the findings of the XRD, XPS, and HRTEM investigations. Additionally, magnetic studies revealed at room temperature, the nanocomposite exhibited superparamagnetic properties. Electrochemical Impedance Spectroscopy (EIS) was employed to characterize the ability of the Fe₃O₄-ZnO:V nanocomposites to transfer electrons. Furthermore, the impact of dopant on optical characteristics was evaluated. When exposed to rhodamine B (RhB), all the samples exhibited photocatalytic activity. Through the use of an ESR experiment and the spin-trapping technique, the existence of reactive oxygen species (ROS) at the solid–liquid interface was demonstrated, and their impact on the samples' photocatalytic activity was highlighted. After recycling, XRD, XPS, and SEM were performed to illustrate the stability of the material. The impact of V doping on the morphologic, structural, and compositional properties of magnetically separable Fe₃O₄-ZnO:V composite nanoparticles for photocatalytic applications is the innovative aspect of our work.

Keywords: photocatalysis; Fe₃O₄; ZnO:V; magnetic recoverable photocatalysts



Citation: Varadi, A.; Leostean, C.; Stefan, M.; Popa, A.; Toloman, D.; Pruneanu, S.; Tripon, S.; Macavei, S. Fe₃O₄-ZnO:V Nanocomposites with Modulable Properties as Magnetic Recoverable Photocatalysts. *Inorganics* **2024**, *12*, 119. <https://doi.org/10.3390/inorganics12040119>

Academic Editor: Antonino Gulino

Received: 4 March 2024

Revised: 29 March 2024

Accepted: 15 April 2024

Published: 17 April 2024



Copyright: © 2024 by the authors. Licensee MDPI, Basel, Switzerland. This article is an open access article distributed under the terms and conditions of the Creative Commons Attribution (CC BY) license (<https://creativecommons.org/licenses/by/4.0/>).

1. Introduction

Nowadays, the extensive use of composites across multiple industrial sectors requires their continued development with respect to both their attributes and their manufacturing techniques [1]. It is possible to produce nanomaterials with remarkable mechanical, optical, electrical, magnetic, and catalytic features that differ considerably from their bulk counterparts. The size, shape, synthesis conditions, and appropriate functionalization can all be accurately managed to provide desired tuning of the aforementioned characteristics [2–4].

One of the most important developments in modern green chemistry is photocatalysis, an environmentally friendly and smart oxidation process. The expansion of photocatalysis as a realistic wastewater treatment technology to eliminate emergent pollutants is a priority for researchers [5–8]. A photocatalyst's band gap energy and electronic band structure, for instance, have a significant impact on its photocatalytic performance. To optimize solar energy consumption, an effective photocatalyst needs to possess a band gap energy of less than 3 eV, which allows for light absorption into the visible spectrum [9–11].

The current photocatalytic system's drawbacks, which restrict its industrial relevance, include its low visible light consumption [12], quick charge recombination [13], and limited

photogenerated electron [14] and hole migration capabilities [15]. Adjustments to the band edge, band gap tuning, and crystal structure may all be applied to boost visible light absorption for the photocatalytic process [13,16].

The remarkable photocatalytic applications of zinc oxide nanostructures, including in the photodegradation of organic contaminants, self-cleaning, and antimicrobial efficiency, are explained by their high specific surface area, optical characteristics, and versatility [7,17,18].

Zinc oxide also has a strong chemical stability, large specific surface area, and low production cost [19]. In a study about the photocatalytic activity of ZnO in degrading the azo dyes, Chen et al. [20] found ZnO photocatalyst prepared with a composite ratio of 4:1 and calcined at 400 °C, displayed a very efficient elimination rate of 99.70% for methyl orange.

Nevertheless, it is also recognized the photocatalyst has several disadvantages as well, including the challenges of agglomerating suspended particles, the difficulty of extracting particles from solution, and the challenge of reusing them for additional applications [21]. It is, however, possible to overcome at least some of these shortcomings and to stimulate their photodegradation abilities by modifying the particles size, varying the morphology, band gap tuning through doping, dual doping, or coupling with other semiconductor nanomaterials [22].

Along with helpful heterojunction that delays charge carrier recombination, the combination of magnetic nanoparticles with semiconductors provides the potential for magnetic recovery at process completion [23]. In semiconductor nanoparticles, doping with different type of metal ions is reported to enhance photocatalytic properties [24–26]. This enhancement is related to their electronic structure and strong emission in the visible light [21,27]. In our specific samples, the spectral response can be shifted towards the visible region by doping with vanadium ions, an intriguing element known for its unique electronic configuration which is an essential attribute in real-world applications [17,28,29]. It is essential to recognize the benefits of UV irradiation in photocatalysis, including its ability to eliminate microbes and its potential application in areas limiting access to sunlight [30,31].

RhB is a popular organic dye in the textile industry, but even at low concentrations, it can have harmful effects on human health and the environment [21,32,33]. Several measures are taken to reduce these negative effects on the environment, one of them being the Fenton method [34].

Wang et al. [35] found Fe₃O₄-ZnO has an increased photocatalytic activity compared to bare ZnO on RhB degradation, due to the higher concentration of surface oxygen vacancies. An efficient and recyclable catalyst combines the magnetic properties of nanoparticles with the semiconducting properties [36] that can be provided by metal oxides [35,37,38]. Also, the bare metal oxides, without any doping metal, showed significantly lower photocatalytic properties, as demonstrated by Ahmad et al. [39] who compared RhB photodegradation by ZnO compared to ZnO@Ag. Other studies in the literature showed complete removal of a RhB solution by Fe₃O₄@SiO₂@TiO₂ after 25 min of UV irradiation, versus Fe₃O₄@SiO₂@TiO₂@Pt after 20 min of UV irradiation [40].

Our goal in this paper is to develop an effective and multifunctional Fe₃O₄-ZnO:V photocatalyst that will contribute to water depollution. The new photocatalyst, designed by adjusting its composition, helps to address the problems regarding currently used photocatalysts: (i) prevent charge carrier recombination; (ii) enhance the usage and absorption of light; and (iii) fast magnetic recovery after utilization. Detailed investigations of Fe₃O₄-ZnO:V composites were conducted to evidence the influence of vanadium ions on morpho-structural, optical, and magnetic properties. The ability to demonstrate the production of ROS helps in understanding the photocatalytic activity.

2. Results and Discussions

2.1. Structural and Morphological Investigations of Fe₃O₄-ZnO:V Nanocomposites

By X-ray diffraction, the structural evaluation of the Fe₃O₄-ZnO:V nanocomposites was carried out. The X-ray diffractograms of Fe₃O₄-ZnO:V nanocomposites, illustrated in

Figure 1, suggested for all prepared samples, the hexagonal ZnO formation was confirmed by diffraction peak values located at 2θ 31.59, 34.48, 47.65, 56.20, 62.83, 67.97, 69.12, 75.59, and 76.86. These peak positions were assigned to the (100), (002), (101), (102), (110), (200), (112), (201), (004), and (202) planes (PDF card No 01-070-8072). Furthermore, the Fe_3O_4 diffraction peaks are shown at $2\theta = 30.15, 35.31, 42.80, 57.08, \text{ and } 65.53$ corresponding to (220), (311), (400), (511), and (440) (PDF card No 01-071-6336).

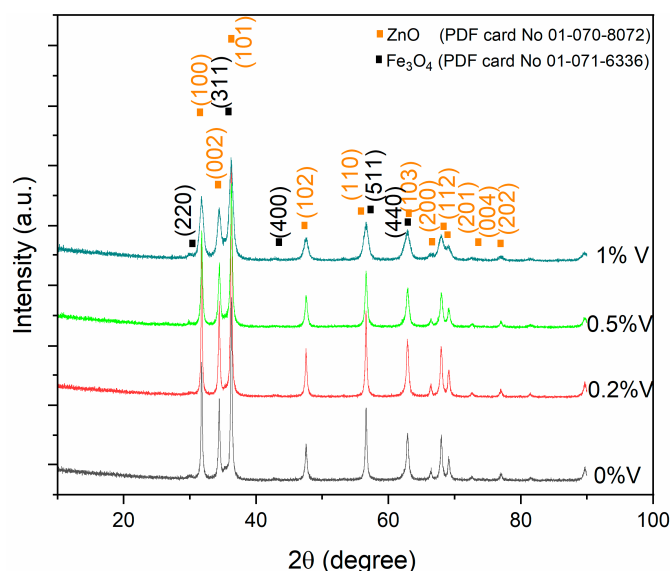


Figure 1. The XRD patterns of $\text{Fe}_3\text{O}_4\text{-ZnO:V}$ nanocomposites and corresponding indexations.

It is important to note the peaks belonging to the magnetic phase of Fe_3O_4 are slightly visible and occasionally overlaid on those of the ZnO crystalline phases due to the high weight ratio $\text{Fe}_3\text{O}_4\text{:ZnO}$ being 1:10. The samples presented no other impurities-associated diffraction peaks.

The XRD line profiles investigation was carried out using the Powder Cell 2.3 program and the Williamson–Hall plot [41] to show the impact of vanadium doping on the ZnO lattice; however, due to the high $\text{Fe}_3\text{O}_4\text{:ZnO}$ 1:10 ratio, only for ZnO is relevant.

Table 1 summarizes the XRD-calculated microstructural parameters, i.e., unit cell parameters, and effective crystallite mean size (D_{eff}).

Table 1. Microstructural parameters of $\text{Fe}_3\text{O}_4\text{-ZnO:xV}$ nanocomposites.

Sample	ZnO				E_g (eV)
	$a = b$ (Å)	c (Å)	V (Å ³)	D_{eff} (nm)	
$\text{Fe}_3\text{O}_4\text{-ZnO:V}$ 0%	3.2467	5.1985	47.45	26.2	3.12
$\text{Fe}_3\text{O}_4\text{-ZnO:V}$ 0.2%	3.2481	5.2038	47.54	29.3	3.15
$\text{Fe}_3\text{O}_4\text{-ZnO:V}$ 0.5%	3.2474	5.2006	47.50	21.1	3.09
$\text{Fe}_3\text{O}_4\text{-ZnO:V}$ 1%	3.2530	5.1860	47.53	11.0	3.03

According to the structural analysis (Table 1), ZnO's lattice parameter c value increases linearly from 5.19 Å (for pure ZnO) to 5.20 Å (for ZnO doped with 0.5% V). The smaller Zn ions (ionic radius 0.74 Å) in the hexagonal ZnO lattice are substituted for larger V^{3+} ions (ionic radius 0.93 Å), as confirmed by the increase in parameter value. As expected, the unit cell volume increases by doping. In contrast, the D_{eff} varies between 11 and 29.3 nm. The primary cause of the decrease in crystallite size is the doping ions' deformation of the host ZnO lattice. And, the vanadium ions' presence slows down the nucleation and subsequent growth of ZnO nanoparticles [42].

Regarding the morphology of $\text{Fe}_3\text{O}_4\text{-ZnO:V}$ nanocomposites, Figure 2 displays TEM images of $\text{Fe}_3\text{O}_4\text{-ZnO:V}$ 0.2% (Figure 2a,b) and $\text{Fe}_3\text{O}_4\text{-ZnO:V}$ 1% (Figure 2c,d) samples at two different resolutions. These images depict clusters of 12 to 15 nm Fe_3O_4 surrounded by 20 to 50 nm diameter ZnO nanoparticles. The sizes correspond with the XRD observations.

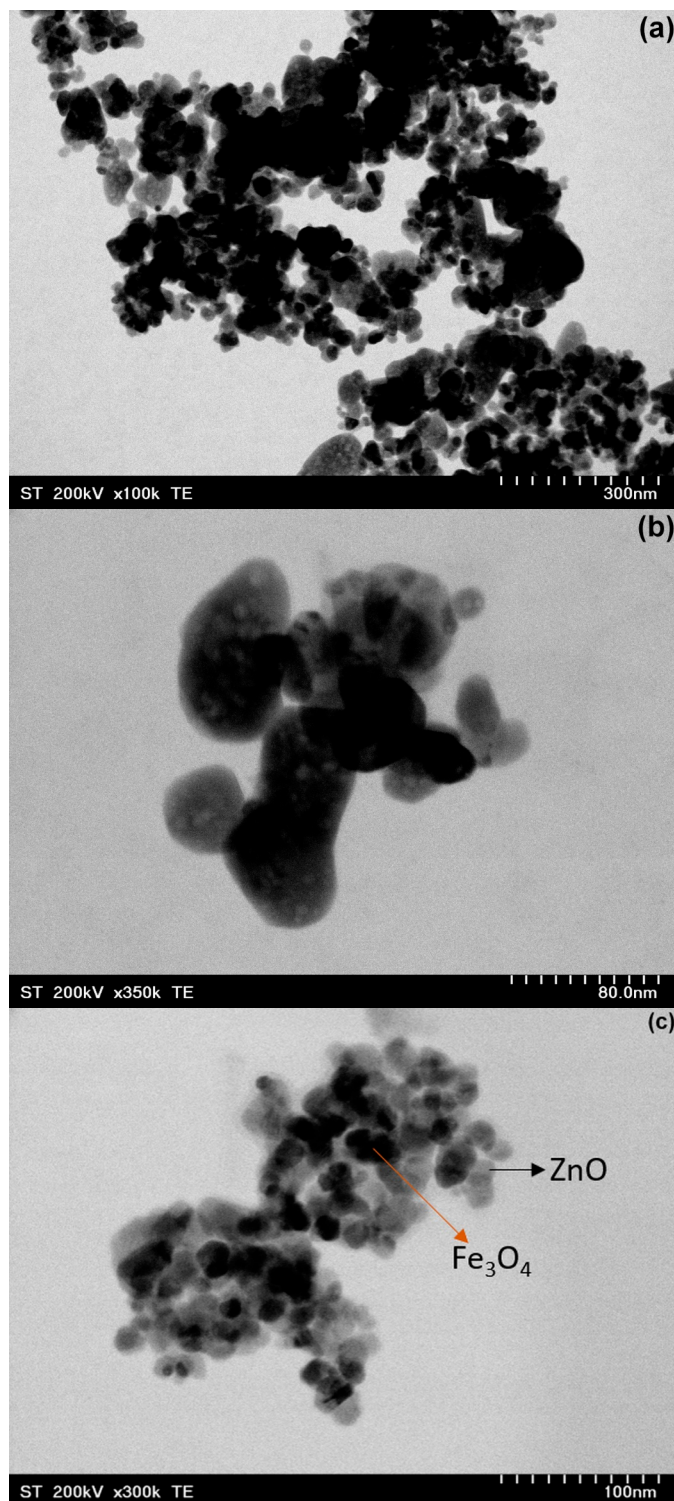


Figure 2. Cont.

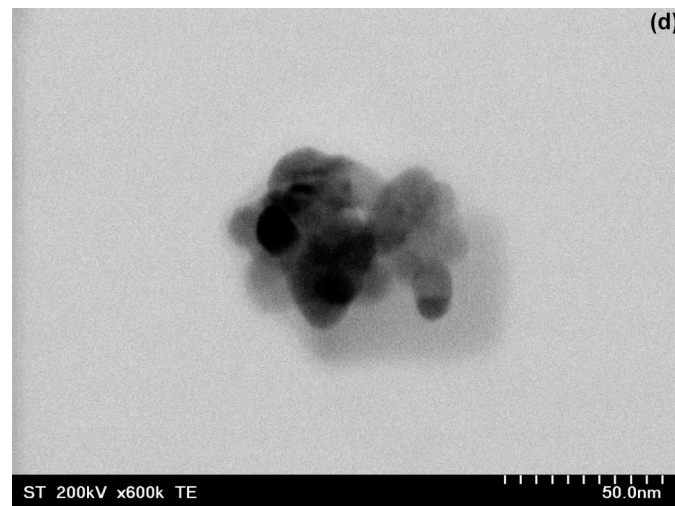


Figure 2. TEM images of (a,b) $\text{Fe}_3\text{O}_4\text{-ZnO:V}$ 0.2% and (c,d) $\text{Fe}_3\text{O}_4\text{-ZnO:V}$ 1% nanocomposites.

Additionally, EDX elemental mapping coupled with TEM analysis was utilized to show the chemical composition of $\text{Fe}_3\text{O}_4\text{-ZnO:V}$ 1% sample. Figure 3a–e indicates the distributions of Zn, Fe, O, and V, supporting the presence of ZnO and Fe_3O_4 in the composite structure. Vanadium mapping is at the equipment's limit of detection, while N is present due to residuals.

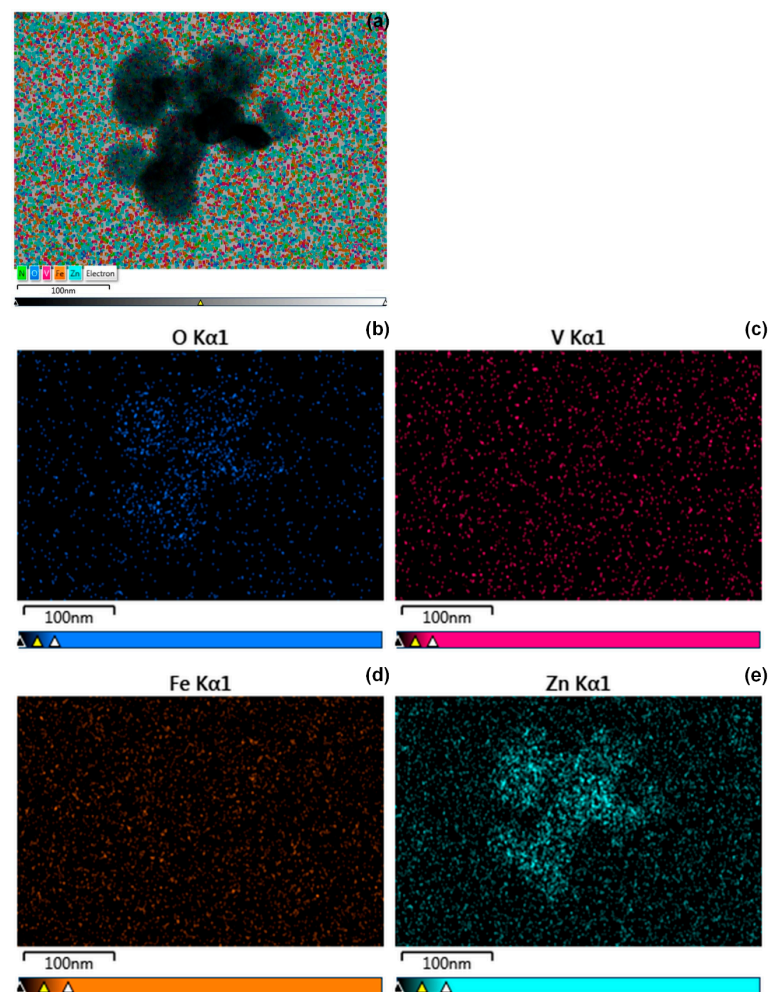


Figure 3. EDX mapping (a–e) of $\text{Fe}_3\text{O}_4\text{-ZnO:V}$ 1% nanocomposite.

2.2. Optical Properties of Fe₃O₄-ZnO:V Nanocomposites

An essential feature of nanocomposites utilized in water purification technologies is their optical properties. Using UV-Vis absorption spectroscopy, the optical characteristics of Fe₃O₄-ZnO:V nanocomposites were investigated, as depicted in Figure 4. Considering the optical properties of the composite nanostructure are a cumulative contribution of each component, our samples absorb light in both the visible and ultraviolet spectrum [43]. The absorbance peaks of each composite sample were detected at 265, 360, and 500 nm, respectively. The origin of these peaks is still controversial, being related to the nanosized nature of samples, defects, and electronic transitions [44,45].

When comparing the absorbance spectra of Fe₃O₄-ZnO:V nanocomposites to samples without a dopant, there is a noticeable enhancement in the visible region absorption at around 500 nm [46]. Because of the presence of V ions in a hexagonal ZnO lattice, this type of absorption behavior is connected to electronic transitions.

Additionally, the absorption spectra show the doping degree has significantly boosted the absorption features for both the visible and ultraviolet regions. Moreover, for doped materials, a clear redshift in the absorption edge at ~380 nm was found. This could be the result of modifications to their surface microstructures and particle sizes [45].

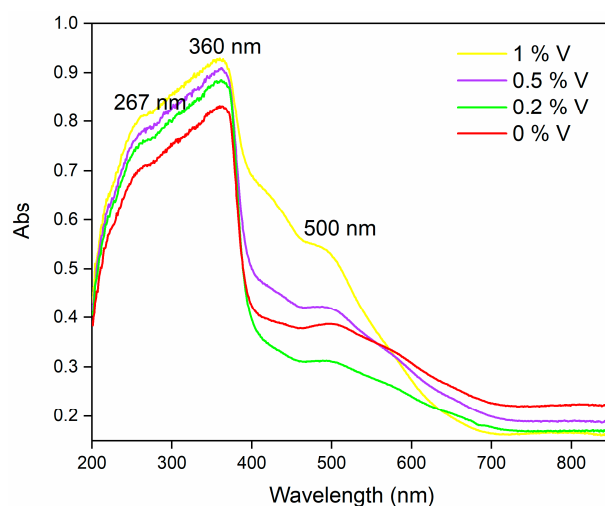


Figure 4. UV-Vis absorption spectra of Fe₃O₄-ZnO:V nanocomposites.

The charge carrier behavior is known to be highly dependent on the photocatalyst's energy band gap (E_g). Since ZnO is a direct band gap semiconductor, the following equations were used to determine the energy band gap values (E_g) of the samples:

$$(\alpha h\nu)^2 = A (h\nu - E_g) \quad (1)$$

where $h\nu$ is the photon energy and α is the absorption coefficient. The band gap values (Table 1) for these doped samples were found to be 3.12 eV (0%), 3.15 eV (0.2%), 3.09 eV (0.5%), and 3.03 eV (1%). A similar lowering of the gap was noted by earlier studies [47].

For the purpose of obtaining more specific information regarding the recombination efficiency of produced hole and electron pairs in Fe₃O₄-ZnO:V nanocomposites, photoluminescence spectroscopy was used, as depicted in Figure 5.

The PL of Fe₃O₄-ZnO and Fe₃O₄-ZnO:V nanocomposites were recorded at room temperature at an excitation wavelength of 220 nm. A combination of several recombination sites and defects in the vacancy level of oxygen and zinc [48,49] could constitute the reason for the broad and varied intensity of PL peaks. The emissions of green, blue, and violet correlate with these peaks. In our sample, it is possible to connect the broad and weak violet emission peak, detected at 426 nm, to the energy required for electrons to move from the conduction band to the interstitial oxygen (O_i). As shown in Figure 5, the emission of this peak is quenching proportionally with the vanadium concentration. The peak around

506 nm indicates the similar behavior of the PL intensity, responsible for the transition from interstitial Zn (Zn_i) to O_i [50]. When the electron and hole combine together to produce a photon, the photocatalytic activity's effect decreases. Therefore, the stronger photocatalytic activity is indicated by the lower PL intensity.

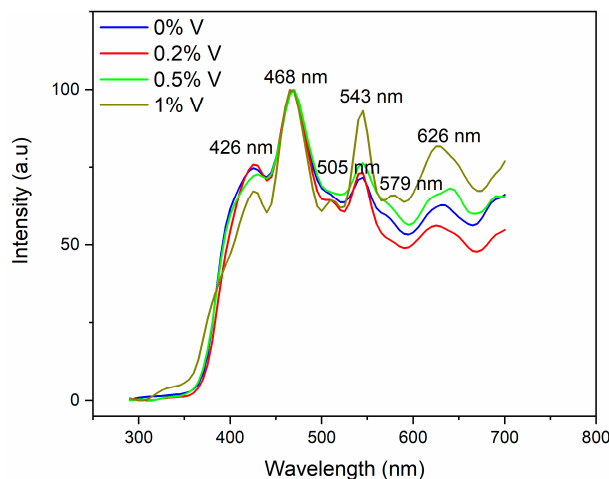


Figure 5. PL spectra characteristic to the Fe_3O_4 -ZnO:V nanocomposites. Excitation at 220 nm.

The origin of PL emission features is still controversial but, generally, they are attributed to the so-called self-activated centers and defects such as oxygen vacancies (V_o), which support the analysis of the magnetic data.

2.3. Compositional Analysis by XPS

The XPS qualitative and quantitative elemental analysis was carried out by recording the Fe 2p, Zn 2p, Zn LMM, V 2p, O 1s, and C 1s core-level lines.

As an example, for sample 1% V, in Figure 6a one can see the Zn 2p core-level spectra were deconvoluted with two peaks positioned at $2p_{3/2}$ 1021.4 and Zn $2p_{1/2}$ 1044.5 eV, assigned to Zn^{2+} . The observed lower BE values than the expected bulk 1022 eV, are characteristic of oxygen deficiency [51]. Also, two satellite peaks positioned at 1022.7 and 1046.1 eV were used.

The Fe 2p core-level line deconvolution, corresponding to sample 1% V, is shown in Figure 6b. One can see the Fe_3O_4 model was applied with the peaks Fe^{2+} $2p_{3/2}$ positioned at 710 eV and Fe^{3+} $2p_{3/2}$ positioned at 711.3 eV. Due to the Mg anode X-ray source the O KLL line is also present in the spectrum. The obtained surface atomic ratio Fe/Zn is 0.08.

The V 2p core-level line deconvolution, corresponding to sample 1% V, is shown in Figure 6c. The peaks positioned at 516.7 eV ($2p_{3/2}$) and 524.1 eV ($2p_{1/2}$) are characteristic to V^{3+} . Due to the non-monochromatic Mg anode X-ray source two satellite peaks also appear in the spectrum [52]. The obtained surface atomic ratio V/Zn is 0.01.

The O1s spectra for ZnO always have two peaks with the one at higher binding energies at ~532 eV attributed to $Zn(OH)_2$ or oxygen vacancies. For more accurate interpretation, three peaks deconvolution can be used with constraints for the position of the O- V_o peak at ~1 eV higher than O-Zn peak [53]. In Figure 6d, the peak positioned at 530 eV is allocated to metal bonded O^{2-} ions, at 531 eV is allocated to O vacancies, and at 532.1 eV is allocated to loosely bound O ions from H_2O . One can see the V_o peak is increasing with V doping. The V_o /O-metal ratio is shown in Table 2.

Zn LMM Auger can be used to obtain information on Zn defects [54]. In Figure 6e, the Zn LMM Auger spectra was deconvoluted with two peaks attributed to Zn in Zn-O (KE 987.8 eV) and the shoulder peak Zn from interstitial sites (Zn_i) (KE 991.1 eV). The ratio of the peaks area, listed in Table 2, indicates V doping increases Zn defects in ZnO by over 50%. In case of sample 0.5% V, the number of Zn_i is slightly lower than in the undoped sample, leading to higher than expected saturation magnetization (Table 2).

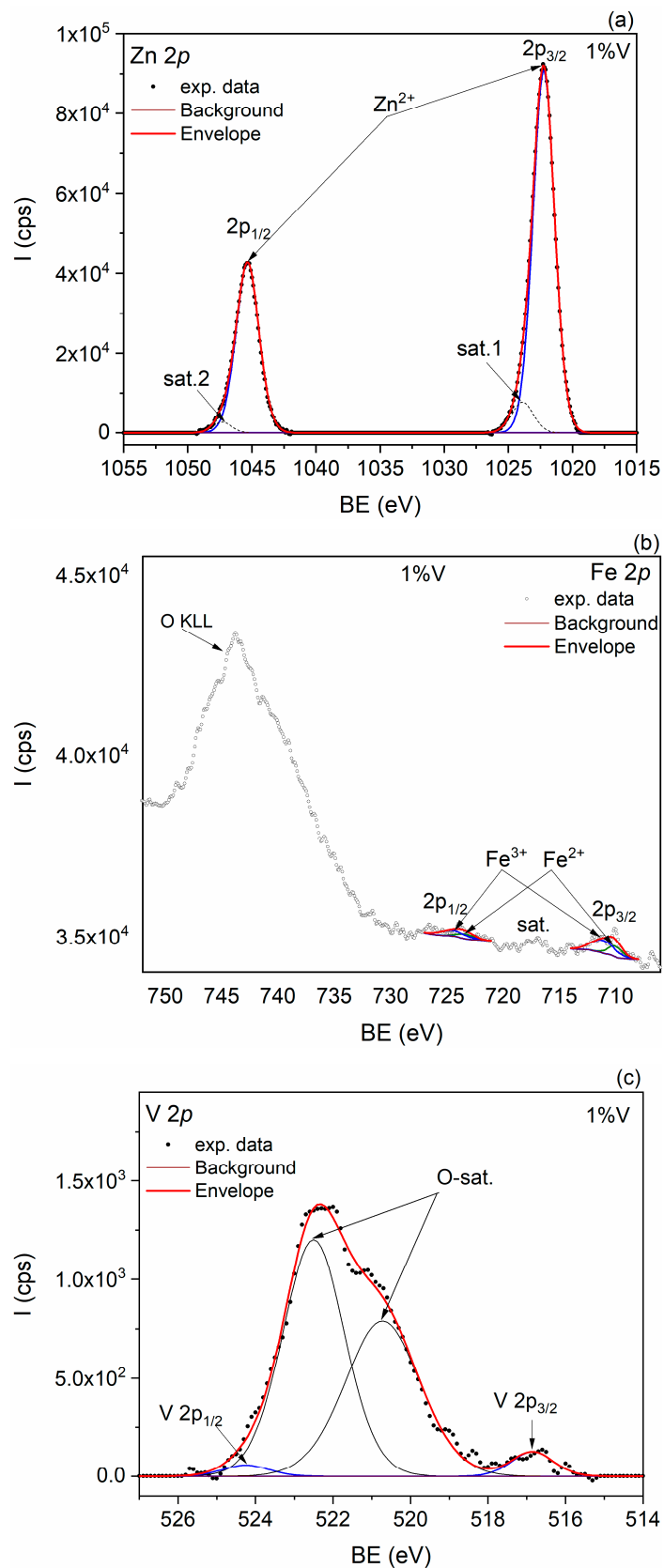


Figure 6. Cont.

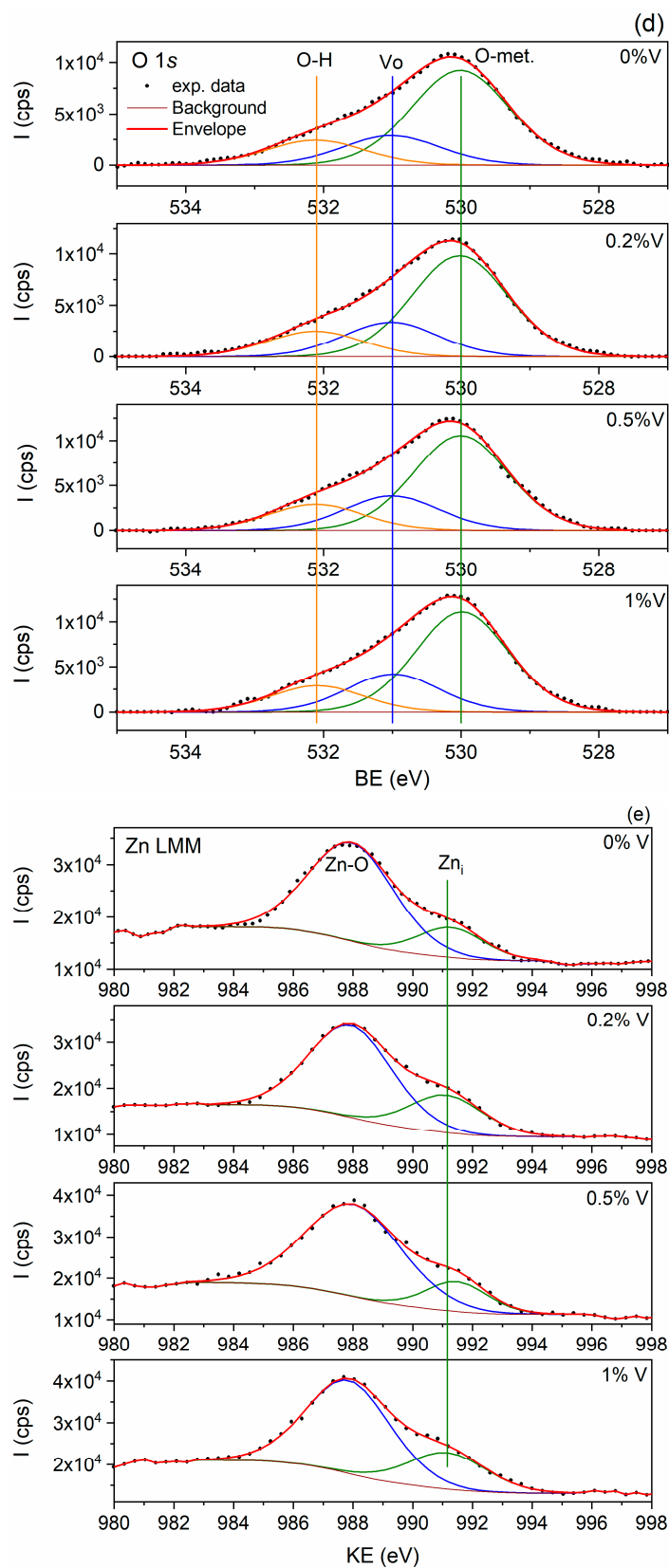


Figure 6. XPS spectra deconvolution of (a) Zn 2p, (b) Fe2p, (c) V2p core-level corresponding to sample 1% V and comparison of (d) O1s core-level and (e) Zn LMM Auger for all Fe_3O_4 -ZnO:V nanocomposites.

Table 2. Vo/O-metal and Zn_i/ZnO atomic ratio determined from XPS.

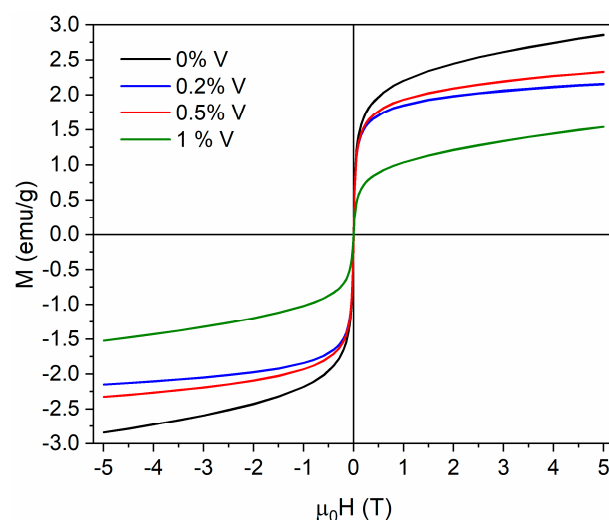
Sample	O1s Vo/O-Metal Ratio	Zn LMM Zn _i /ZnO Ratio
Fe ₃ O ₄ -ZnO:V 0%	0.31	0.23
Fe ₃ O ₄ -ZnO:V 0.2%	0.34	0.35
Fe ₃ O ₄ -ZnO:V 0.5%	0.36	0.20
Fe ₃ O ₄ -ZnO:V 1%	0.37	0.36

2.4. Magnetic Characterization of Fe₃O₄-ZnO:V Nanocomposites

Room temperature magnetization curves are shown in Figure 7. The Fe₃O₄-ZnO sample saturation magnetization (Ms) value 3.3 emu/g indicates it can be used for magnetic separation, similar to other publications [48,55].

By V doping Ms decreases to 1.9 emu in case of 1% V. This behavior was observed in theoretical studies and explained by irregular distribution of V atoms [56] and/or Zn defects [57].

Also, by V doping, the coercive field (Hc) value remains almost constant at ~20 Oe, while the remanent magnetization (Mr) decreases from 0.1 (sample Fe₃O₄-ZnO) to 0.03 emu/g (sample Fe₃O₄-ZnO 1% V), indicating a superparamagnetic behavior.

**Figure 7.** Room temperature magnetization of Fe₃O₄-ZnO:V nanocomposites.

The values of Ms, Hc, and Mr for Fe₃O₄-ZnO and V-doped samples are shown in Table 3. Ms does not decrease linearly with V doping. In accordance with XRD (lower unit cell volume and Deff for sample 0.5% V) and XPS (lower Zn_i/ZnO ratio for sample 0.5% V), this shows the Zn defects' influence on magnetic properties, similar to [58].

Table 3. Ms, Hc, and Mr values for Fe₃O₄-ZnO:V nanocomposites.

Sample	Ms (emu/g)	Hc (Oe)	Mr (emu/g)
Fe ₃ O ₄ -ZnO:V 0%	3.3	20	0.1
Fe ₃ O ₄ -ZnO:V 0.2%	2.3	20	0.09
Fe ₃ O ₄ -ZnO:V 0.5%	2.5	21	0.09
Fe ₃ O ₄ -ZnO:V 1%	1.9	20	0.03

2.5. Photocatalytic Properties

To evaluate the photocatalytic activity of the prepared samples, the RhB pollutant degradation was monitored under UV light irradiation (365 nm). All samples show similar adsorption capacity, the equilibrium adsorption-desorption been reached after 60 min in the dark. Figure 8 displays the efficiency of RhB removal from the solution by the synthesized samples. The removal rates vary between 38% for Fe₃O₄-ZnO and 95% for Fe₃O₄-ZnO:V 1%.

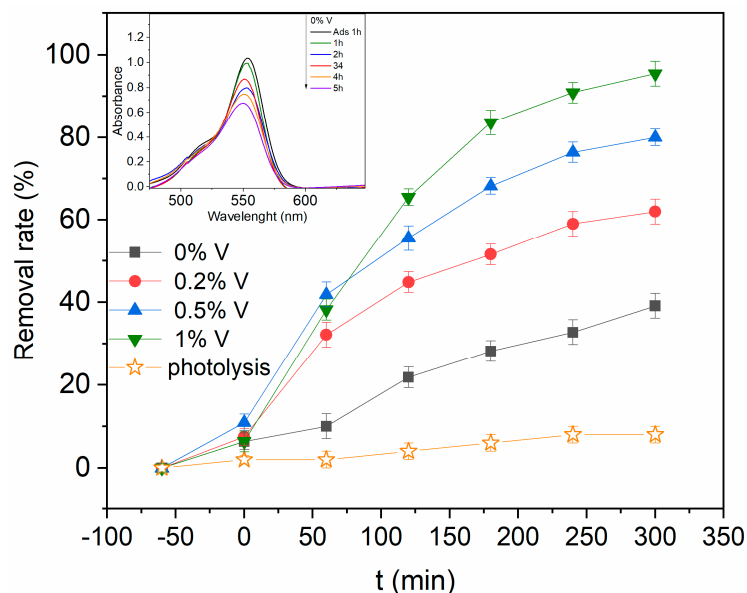


Figure 8. Photocatalytic degradation of RhB and in the presence of Fe₃O₄-ZnO:V nanocomposites. The insert presents the UV–vis absorption spectra of RhB aqueous solution in the presence of Fe₃O₄-ZnO 0% V at different irradiation time intervals. The error bars indicate the standard deviations ($n = 3$).

The first-order kinetic model was applied to evaluate the photocatalytic activity:

$$-\ln\left(\frac{C_t}{C_0}\right) = k_i x t \quad (2)$$

where C_t represents the concentration of RhB at t time; C_0 —concentration of RhB after adsorption in dark; t —irradiation time; and k_i —apparent kinetic constant. The obtained results are shown in Figure 9, and a linear dependence with the irradiation time can be observed. After the linear fitting of the curves, the k_i and R^2 parameters are obtained (Table 4).

Table 4. The apparent first-order rate constant, k of photocatalytic degradation, and correlation coefficient, R^2 .

Sample	Fe ₃ O ₄ -ZnO:V 0%	Fe ₃ O ₄ -ZnO:V 0.2%	Fe ₃ O ₄ -ZnO:V 0.5%	Fe ₃ O ₄ -ZnO:V 0.7%	Fe ₃ O ₄ -ZnO:V 1%
$k_i \times 10^{-3} \text{ (min}^{-1}\text{)}$	1.5	2.97	4.97	2.36	10.3
R^2	0.97	0.94	0.98	0.99	0.99

It can be observed by increasing the V doping degree, the apparent kinetic constant increases from $1.5 \times 10^{-3} \text{ min}^{-1}$ (for Fe₃O₄-ZnO:V 0%) to $10.3 \times 10^{-3} \text{ min}^{-1}$ (for Fe₃O₄-ZnO:V 1%). These results sustained the conclusion that Fe₃O₄-ZnO:V 1% sample had the best photocatalytic activity. Based on the XPS results, these assumptions support V doping increases V_o .

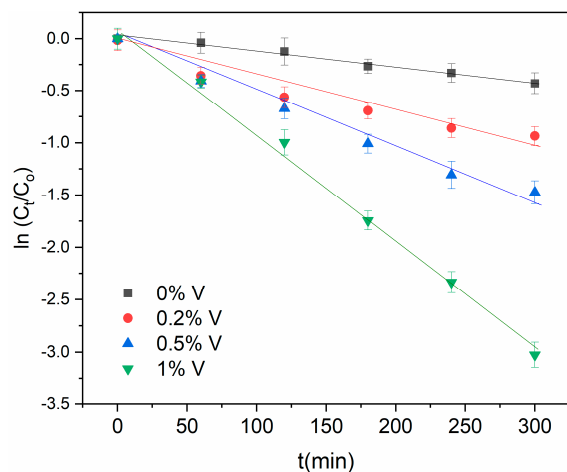


Figure 9. Evaluation of the photodegradation kinetic. The error bars indicate the standard deviations ($n = 3$).

2.5.1. Effect of the Solution pH on Pollutant Elimination

The RhB solution pH was varied between 2 and 11. The photodegradation was performed in the presence of $\text{Fe}_3\text{O}_4\text{-ZnO:0.5\% V}$ nanoparticles. This system was chosen because it presented the best photocatalytic activity. The obtained results are shown in Figure 10a, and it can be seen the highest photocatalytic activity is obtained using acidic to neutral solution.

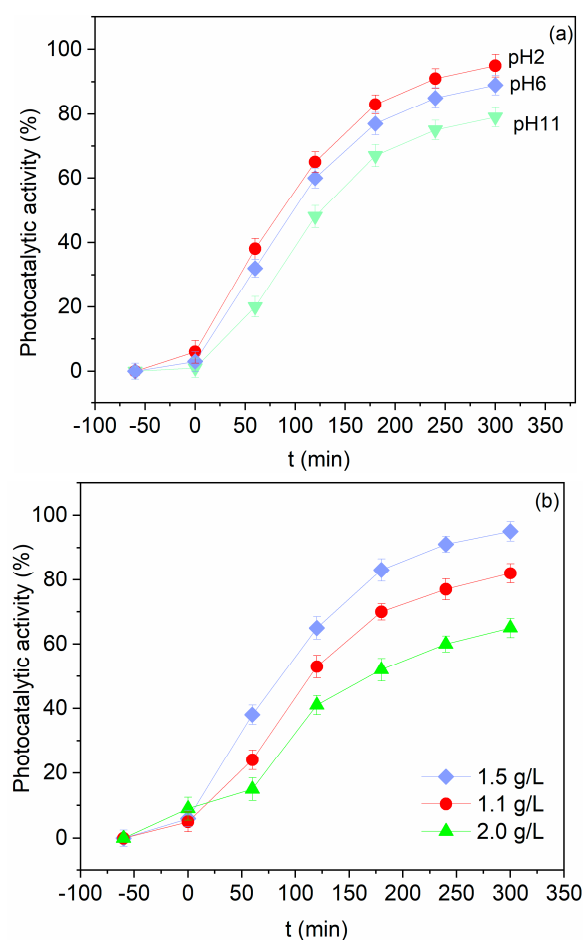


Figure 10. (a) Effect of initial solution pH on RhB photodegradation. (b) Effect of $\text{Fe}_3\text{O}_4\text{-ZnO:0.5\% V}$ photocatalyst concentration on RhB photodegradation. The error bars indicate the standard deviations ($n = 3$).

When the photocatalytic activity takes place in a basic solution (pH ~ 11), probably a repulsion appears between the nanoparticles and pollutant molecules, both being loaded with a negative charge [59]. This effect reduces the contact between the nanoparticles and the pollutant molecules, driving the photocatalytic activity reduction.

2.5.2. Effect of Photocatalyst Dosage

At pH 6, the photocatalyst amount was varied between 1.1 g/L and 2.0 g/L. As can be seen in Figure 10b, an increase in the photocatalytic activity with the photocatalyst amount is followed by a decrease at higher amounts.

Therefore, an optimal photocatalyst concentration exists that ensures more efficient absorption of photons as well as better adsorption of pollutant molecules due to the larger specific surface area. By exceeding this amount, due to the solution opacity favorizing the light scattering, the photocatalytic activity decreases [60].

2.6. Reactive Oxygen Species Generation

The generation of reactive oxygen species (ROS) under UV light irradiation was highlighted using the EPR spectroscopy coupled with the spin-trapping technique. The experiment was carried out on the sample with the best photocatalytic activity (Fe₃O₄-ZnO:V 1%), Fe₃O₄, and ZnO:V 1% nanoparticles. Before irradiation, no EPR spectrum was obtained for all analyzed samples. After 10 min of UV (365 nm) light irradiation, complex spectra composed of several absorption lines were evidenced as shown in Figure 11a–c. To identify the components, a spectra simulation was performed. The simulation of the Fe₃O₄-ZnO:V 1% and ZnO:V 1% spectra indicates the presence of the same spin adducts namely: •DMPO-OOH (aN = 13.8 G, aH = 11.8, aH = 0.9 G, g = 2.0098), •DMPO-O₂^{•-} (aN = 12.8 G, aH = 10.4 G, aH = 1.4 G), •DMPO-N (aN = 14 G), and •DMPO-CH₃ (aN = 15.5 G, aH = 22.3 G).

In the case of the spectrum corresponding to Fe₃O₄ nanoparticles, the simulation was performed considering only the following two components: •DMPO-OOH (aN = 13.8 G, aH = 11.8, aH = 0.9 G, g = 2.0098) and •DMPO-O₂^{•-} (aN = 12.8 G, aH = 10.4 G, aH = 1.4 G). The generation of the highlighted ROS can be described by the following equations [61]



The last component evidenced in the simulation of Fe₃O₄-ZnO:V 1% and ZnO:V 1% spectra corresponds to nitroxide-like radical which occurs by breaking C-N bond of DMPO [61].

Consequently, both O₂^{•-} and •OH radicals are formed during Fe₃O₄-ZnO:V 1% and ZnO:V 1% sample irradiation, O₂^{•-} being the main species as shown by the higher intensity of the corresponding spectrum. On the contrary, in the case of Fe₃O₄, only O₂^{•-} is generated.

Based on the above results, a photocatalytic mechanism is proposed as illustrated in Figure 12. During the irradiation e⁻-h⁺ pairs are generated in both components of the composite material. The photoexcited electrons from the Fe₃O₄ conduction band (CB) are transferred to CB of ZnO, characterized by a lower energy. Its interaction with the surface-adsorbed O₂ drives generation of the •O⁻² radicals. Simultaneously, the holes from the ZnO valence band (VB) will migrate to the VB of Fe₃O₄. However, since the VB potential of Fe₃O₄ is lower compared with the oxidation potential of OH⁻/•OH and H₂O/•OH redox pairs, these reactions cannot occur [62]. Therefore, only the remaining holes from the VB of ZnO will interact with H₂O molecules generating •OH radicals.

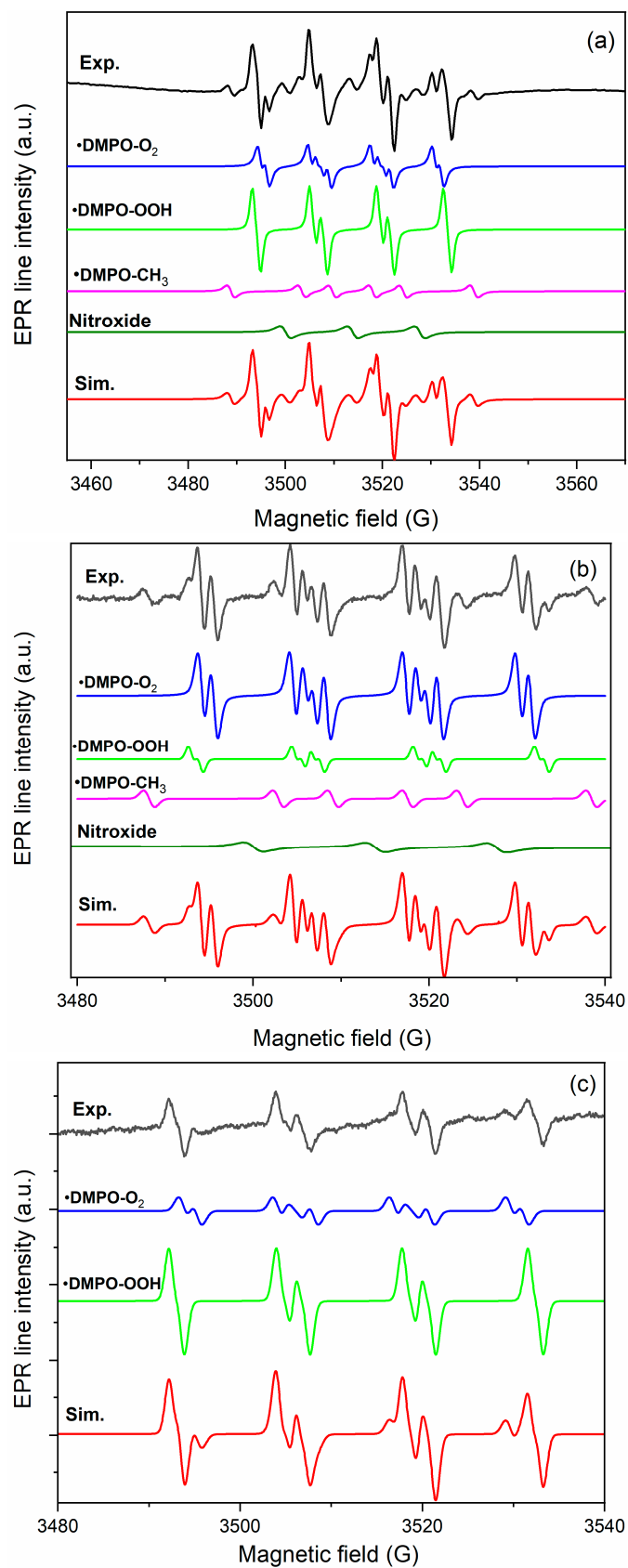


Figure 11. Simulated spectra of DMPO spin adducts generated by (a) Fe₃O₄-ZnO:V 1%, (b) ZnO:V 1%, and (c) Fe₃O₄ samples after UV irradiation.

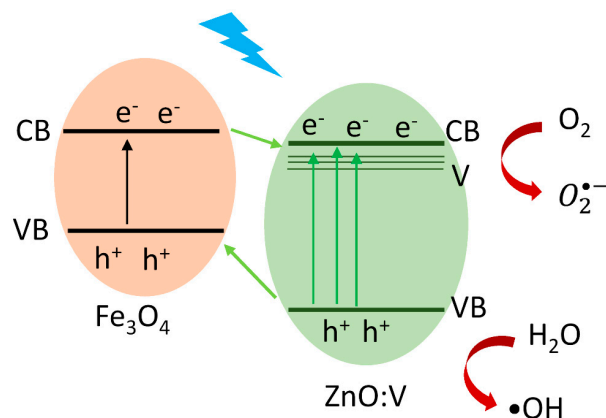


Figure 12. Photodegradation mechanism mediated by Fe_3O_4 - $\text{ZnO}:\text{V}$ nanocomposites.

2.7. Stability Tests

To evaluate the reuse of the prepared photocatalysts, five degradation cycles were carried out under similar conditions. Before reuse, the material was recovered from the solution using a magnetic field, after which it was washed with distilled water and dried. It can be seen the degradation efficiency does not change substantially after the cycles performed (Figure 13a).

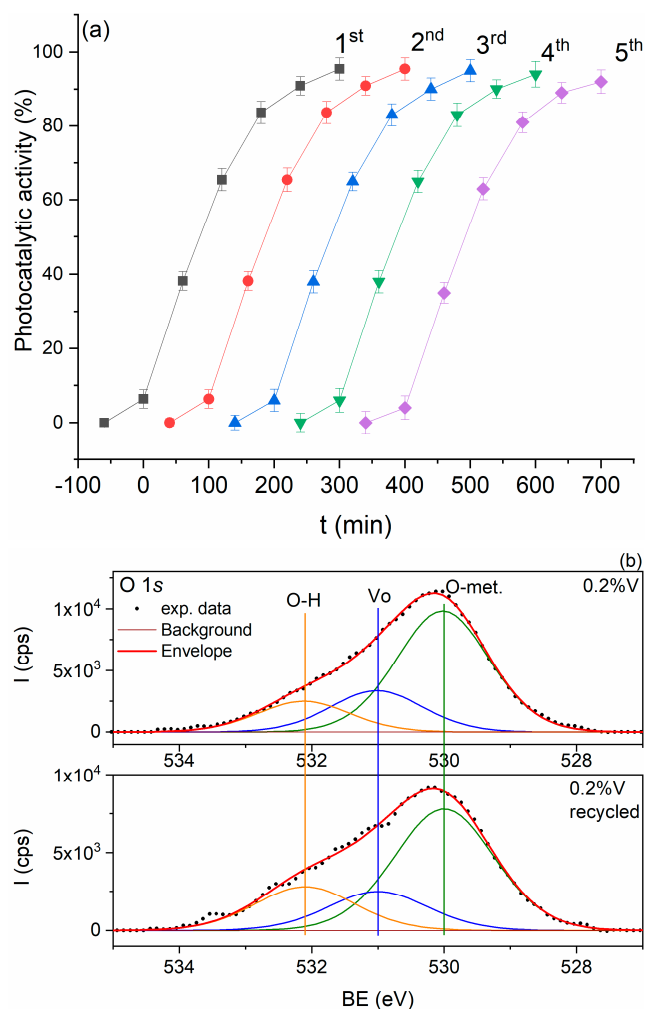


Figure 13. Cont.

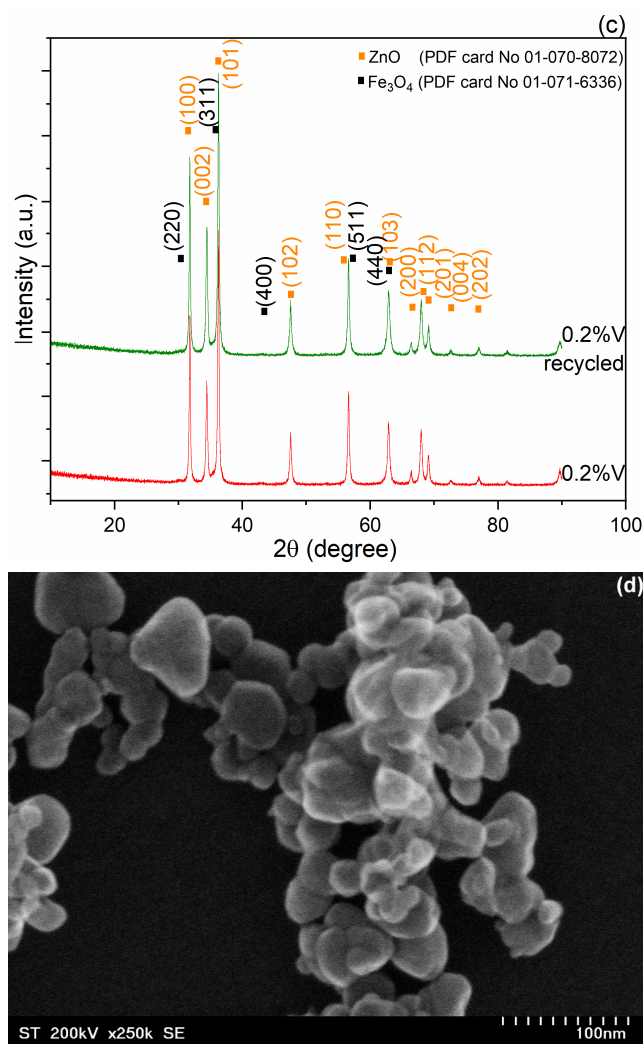


Figure 13. (a) Photocatalyst stability test of the $\text{Fe}_3\text{O}_4\text{-ZnO:V}$ 1% nanocomposites for the photodegradation of RhB. (b) XPS spectra deconvolution of O1s core-level for $\text{Fe}_3\text{O}_4\text{-ZnO:0.2\% V}$ sample before and after recycling. (c) The XRD patterns of $\text{Fe}_3\text{O}_4\text{-ZnO:0.2\% V}$ sample before and after recycling. (d) SEM image corresponding to recycled $\text{Fe}_3\text{O}_4\text{-ZnO:0.2\% V}$ sample.

To demonstrate the stability of the material, XPS (Figure 13b), XRD patterns (Figure 13c), and SEM (Figure 13d) spectra of $\text{Fe}_3\text{O}_4\text{-ZnO:V\%}$ nanocomposites after the photocatalysis reaction were performed. The XPS O1s Vo/O-metal ratio slightly decreased from 0.34 to 0.32 after recycling, while the Zn LMM Zni/ZnO ratio also slightly decreased from 0.35 to 0.31 after recycling. Also, as expected, after recycling the absorbed water content on the sample 0.2% V surface increased by 44% from 0.25 to 0.36, calculated from O1s O-H/O-metal ratio. Since XPS is a surface-sensitive technique one can conclude the material is stable after recycling. Furthermore, the XRD pattern for the same sample after RhB degradation suggests the composite samples do not have any additional secondary phases. There are no obvious modifications to the crystallite size. In addition, no noticeable modification was observed in the SEM images (Figure 13d).

2.8. Electrochemical Studies

Electrochemical Impedance Spectroscopy (EIS) was employed to characterize the ability of the modified electrodes to transfer the electrons across the solution/electrode interface. The technique can provide information about the charge transfer resistance (R_{ct}) of various materials by applying a small sinusoidal signal (5 mV) of various frequencies

(0.1–105 Hz). In this case, we compared the EIS spectra (Nyquist plots) of the two modified electrodes (Figure 14).

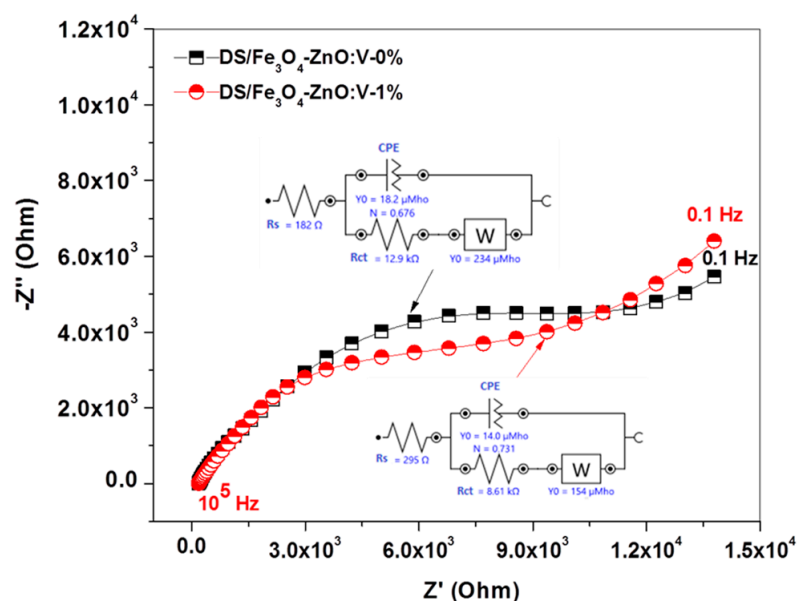


Figure 14. Nyquist plots of the modified electrodes, recorded in solution containing 10^{-3} M potassium ferrocyanide and 0.2 M KCl; 0.1–105 Hz frequency range. Insert: the equivalent electrical circuits employed to fit the Nyquist plots of the modified electrodes.

The recorded spectra were interpreted based on the equivalent electrical circuit, which model each spectrum (see the circuits in the insert). In both cases, the recorded EIS spectra are characterized by a large semi-circle in the high-medium frequency range, attributed to the charge-transfer resistance (R_{ct}) of the material. At low frequencies, a straight line can be observed, describing the diffusion of the redox species within the double-layer (Warburg impedance (W)). At the electrode/solution interface, the accumulation of ions generally takes place, leading to the charging of the double-layer; this was modeled by a constant phase element (CPE) and not by a pure capacitance, due to the porous morphology of the surface. In addition, the circuits contain the electrolyte resistance (R_s), which has a low value due to the good conductivity of the solution. It is interesting to see in the case of $\text{Fe}_3\text{O}_4\text{-ZnO:V-1\%}$ material, the R_{ct} value is 8.61 k Ω , being considerably lower than that corresponding to the $\text{Fe}_3\text{O}_4\text{-ZnO:V-0\%}$ material (12.9 k Ω). This indicates the material containing 1% vanadium ($\text{Fe}_3\text{O}_4\text{-ZnO:V 1\%}$) is more efficient for the transfer of electrons, in comparison with $\text{Fe}_3\text{O}_4\text{-ZnO:V 0\%}$ nanocomposite.

This behavior was further confirmed by testing the electrodes modified with the two materials for the oxidation of RhB, in the presence and absence of visible irradiation (Figure 15). The halogen lamp used for photocatalytic experiments was also employed as irradiation source.

As shown in Figure 15, a well-defined oxidation peak was recorded in 10^{-4} M RhB solution at a potential of +0.85 V (black curve) with $\text{DS/Fe}_3\text{O}_4\text{-ZnO:V 0\%}$ electrode, and slightly increased for $\text{DS/Fe}_3\text{O}_4\text{-ZnO:V 1\%}$ (blue curve; both in dark conditions). After illumination with visible light, the current density and hysteresis in the CV curve were considerably higher for the $\text{DS/Fe}_3\text{O}_4\text{-ZnO:V 1\%}$ electrode. This result suggests the photocatalytic activity of $\text{Fe}_3\text{O}_4\text{-ZnO}$ may be considerably improved by doping with low amounts of vanadium (1%), which leads to smaller charge transfer resistance and consequently easy transfer of charge.

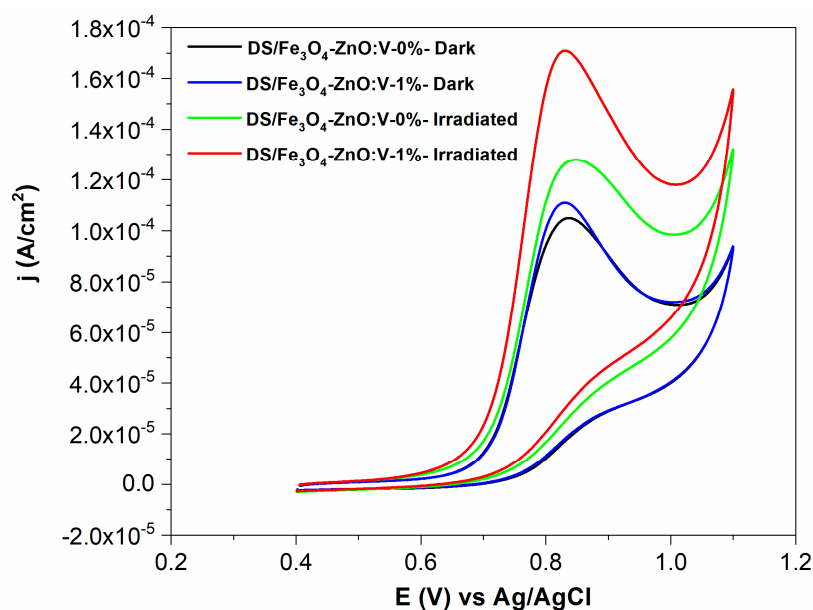


Figure 15. CVs recorded in dark and visible irradiations with DS/Fe₃O₄-ZnO:V 0% electrode and DS/Fe₃O₄-ZnO:V 1% in solution containing 10⁻⁴ M RhB and 0.2 M KCl at 10 mV/s scanning rate.

3. Experimental Part

3.1. Materials

To synthesize Fe₃O₄-ZnO:V composite nanoparticles, the following chemical reagents were used: FeCl₃ × 6H₂O (98% Alfa Aesar, Ward Hill, MA, USA), FeCl₂ × 4H₂O (98% Alfa Aesar), NH₃ (25% Merck, Darmstadt, Germany), zinc acetate—Zn(CH₃COO)₂ × 2H₂O (Alfa Aesar), diethylene glycol—C₄H₁₀O₃ (VWR, Radnor, PA, USA), and sodium metavanadate—NaVO₃ (Alfa Aesar). All compounds are analytical grade and were used just as supplied, without additional purification.

3.2. Sample Preparation

The synthesis of Fe₃O₄ nanoparticles and their subsequent decorating with ZnO:V nanoparticles were the two steps involved in the synthesis of the Fe₃O₄-ZnO nanocomposites.

The co-precipitation method [2] was implemented to produce the Fe₃O₄ nanoparticles, with a few minor adjustments. Initially, a molar ratio of 2:1 was used to stoichiometrically dissolve FeCl₃·6H₂O and FeCl₂·4H₂O into deionized water containing an excess of ammonia until pH = 12 was reached, at 80 °C. After 60 min, the sample was magnetically recovered and completely rinsed with high-purity deionized water. The prepared sample was dried for 24 h at 60 °C.

The sol-gel process was carried out for decorating the ZnO:V nanoparticles onto the preformed magnetite nanoparticles. Under magnetic stirring, 50 mL of diethylene glycol (DEG) was mixed with a set quantity of zinc acetate hexahydrate (Zn(CH₃COO)₂·6H₂O) (98%) in a Berzelius beaker. A few drops of water (1 mL) were added once the reactants had dissolved. To produce a sol, the mixture is heated to 160–180 °C for 10 min, and then allowed to evaporate for 4 h.

Subsequently, Fe₃O₄ nanoparticles that were ultrasonically dispersed were introduced, according to a mass ratio Fe₃O₄:ZnO of 1:10. Then, the process was allowed to continue for an additional four hours at 160–180 °C under magnetic stirring. The resultant product was dried in an oven at 65 °C for 24 h after being separated by centrifugation. The illustration of synthesis process is depicted in Figure 16.

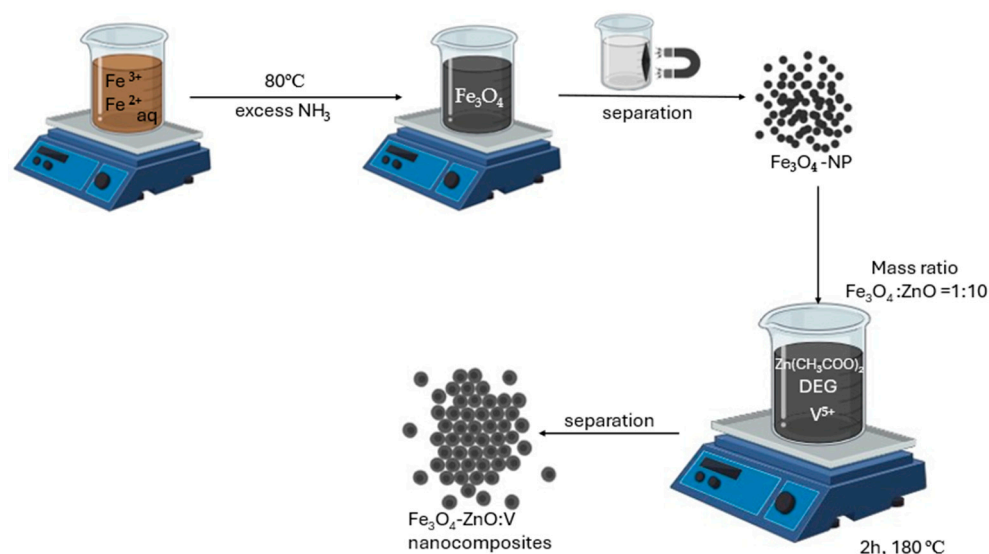


Figure 16. Illustration steps for synthesis of $\text{Fe}_3\text{O}_4\text{-ZnO:V}$ nanocomposites.

3.3. Methods

The crystalline structure of the samples was validated by X-ray diffraction (XRD), which was recorded using a Bruker D8 Advance (Bruker, Karlsruhe, Germany) X-ray diffractometer set up at 40 kV and 40 mA fitted with a germanium monochromator in the incidence. The X-ray diffraction patterns were obtained in the 2θ range of $10^\circ\text{--}80^\circ$ using Cu $K\alpha 1$ radiation ($\lambda = 1.54056 \text{ \AA}$) in a step-scanning mode with increments of $\Delta\theta = 0.02$.

The morphology of the nanocomposites was examined by transmission electron microscopy (TEM), using a Hitachi SU8230 Transmission Electron Microscope (Hitachi, Tokyo, Japan) fitted with a cold field emission gun. By applying a BANDELIN SonOREX homogenizer, the powder was mixed with ethanol and spread out onto a 400 mesh copper grid that had been covered in carbon film.

The qualitative and quantitative chemical composition of the samples was studied with X-ray Photoelectron Spectroscopy (XPS) by using a custom-build SPECS spectrometer with a Mg X-ray source ($h\nu = 1253.64 \text{ eV}$). The samples were drop-cast with ethanol on the sample holder. The CasaXPS software (SPECS, Berlin, Germany, CasaXPS version 2.3.23) was used for spectral analysis with Shirley background subtraction. The integral intensities were calibrated by the corresponding relative sensitivity (RST), transmission (T), and electronic mean free path factors (MFP). Binding energy was corrected by referencing the adventitious C 1s at 284.6 eV.

The magnetic behavior of the samples was investigated with a cryogen-free VSM (CRYOGENIC Ltd., London, UK), using an applied magnetic field up to 5 T at room temperature.

The UV–Vis characterization was realized by JASCO V570 UV–Vis–NIR Spectrophotometer (JASCO Deutschland GmbH, Pfungstadt, Germany) equipped with absolute reflectivity measurement JASCO ARN-475 accessory. The reflectance spectra obtained were transformed into absorbance by the internal software of the spectrophotometer.

Fluorescence emission and excitation spectra were measured using a JASCO FP-6500 spectrofluorometer (JASCO Deutschland GmbH, Pfungstadt, Germany), equipped with a Xe lamp of 150 W, 1800 lines/mm monochromator, and 1 nm spectral resolution.

The photodegradation of Rhodamine B (RhB) was performed in a Laboratory-UV-Reactor system that contains a 400 W halogen lamp (Osram). The irradiance was 0.91 mW/cm^2 at a distance of 25 cm from the sample. The catalyst (10 mg) was dispersed in aqueous solution of RhB ($1.0 \times 10^{-5} \text{ mol L}^{-1}$, 10mL) followed by stirring the mixture in the dark to realize the adsorption equilibrium on the catalyst surface.

The ROS production of $\text{Fe}_3\text{O}_4\text{-ZnO:Vx\%}$ nanocomposites in DMSO (dimethyl sulfoxide) suspensions was investigated by using the Electron Spin Resonance (ESR) coupled with the spin-trapping probe technique. The 5,5-dimethyl-1-pyrroline N-oxide (DMPO,

Sigma–Aldrich, Merck, KgaA, Darmstadt, Germany) was used as spin-trapping agent. The samples were investigated by dispersing 10 mg of Fe₃O₄-ZnO:V 1% in 1 mL of DMSO. These suspensions were homogenized in an ultrasonic bath (30 s) before use. The DMPO concentration was 0.2 M. The experimental and simulated spectra of Fe₃O₄-ZnO:V 1% sample were prepared immediately before measurements and transferred into a quartz flat cell optimized for liquids measurements. The measurements were performed with a Bruker E-500 ELEXSYS X-band (9.52 GHz) spectrometer (Rheinstetten, Baden-Württemberg, Germany) in the same experimental conditions.

Electrochemical measurements (Cyclic Voltammetry (CV); Electrochemical Impedance Spectroscopy (EIS)) were recorded with an AUTOLAB-302N Potentiostat/Galvanostat (Utrecht, The Netherlands) coupled with a screen-printed electrode (DS) and a personal computer. The CV data were recorded with the NOVA 1.11 software. The surfaces of the electrodes were modified with the synthesized materials and were subsequently denoted DS/Fe₃O₄-ZnO:V 1% and DS/Fe₃O₄-ZnO:V 0%, respectively. For surface modification, a volume of 9 µL suspension containing 2 mg/mL Fe₃O₄-ZnO:V-1% or Fe₃O₄-ZnO:V-0% in DMF, was drop-cast on top of each electrode. After that, the modified electrodes were left to dry at room temperature until the next day. The cyclic voltammograms were recorded between +0.4 and +1.1 V versus Ag/AgCl in electrolyte solution containing 10^{−4} M Rhodamine B and 0.2 M KCl supporting electrolyte. The EIS measurements were recorded between 0.1–105 Hz range, in solution containing 10^{−3} M potassium ferrocyanide and 0.2 M KCl. The active areas of DS/Fe₃O₄-ZnO:V 1% and DS/Fe₃O₄-ZnO:V 0% electrodes were determined to be 0.0428 cm² and 0.0483 cm², respectively.

4. Conclusions

For the purpose of water treatment, Fe₃O₄-ZnO:V nanocomposites were synthesized by seed-mediated growth of ZnO:V nanoparticles on preformed magnetite. XRD and TEM were employed to estimate the size, shape, and structure of the nanoparticles. The structural study demonstrates the integration of V ions in the ZnO lattice induces a decrease in particle size. At the same time, optical assessment of Fe₃O₄-ZnO:V nanocomposites revealed the band gap's narrowing by the vanadium ions.

The sample with 1% V exhibits the best photocatalytic activity toward RhB degradation. The existence of V_o and Zn_i increased by V doping is revealed by the XPS data. Magnetization is decreasing by V doping in accordance with Zn_i. According to the EPR data, the main reactive oxygen species (ROS) in the photocatalytic process are both O₂^{•−} and •OH radicals.

The sample shows a significant quenching of PL emission for the highest photocatalytic activity, suggesting stability between electrons and holes (e[−]/h⁺).

EIS showed Fe₃O₄-ZnO:V 1% nanocomposite is more efficient for transferring electrons, in comparison with Fe₃O₄-ZnO:V 0%.

The stability of the material after recycling was confirmed by XRD, XPS, and SEM.

Author Contributions: Conceptualization, A.V., M.S., A.P. and D.T.; Methodology, M.S.; Validation, A.V. and M.S.; Formal analysis, A.V. and C.L.; Investigation, A.V., C.L., A.P., D.T., S.P., S.T. and S.M.; Data curation, A.V., M.S. and S.M.; Writing—original draft, A.V., M.S., A.P., D.T., S.T. and S.M.; Writing—review & editing, A.V., C.L., M.S., A.P. and D.T.; Supervision, A.V., C.L. and M.S. All authors have read and agreed to the published version of the manuscript.

Funding: This research was funded by the MCID through the “Nucleu” Programe within the National Plan for Research, Development and Innovation 2022–2027, project PN 23 24 01 03 and through Program 1—Development of the national research and development system, Subprogram 1.2—Institutional performance—Projects that finance the RDI excellence, Contracts no. 37PFE/30.12.2021.

Data Availability Statement: Data are contained within the article.

Conflicts of Interest: The authors declare no conflict of interest.

References

1. Dicker, M.P.M.; Duckworth, P.F.; Baker, A.B.; Francois, G.; Hazzard, M.K.; Weaver, P.M. Green Composites: A Review of Material Attributes and Complementary Applications. *Compos. Part A Appl. Sci. Manuf.* **2014**, *56*, 280–289. [[CrossRef](#)]
2. Baig, N.; Kammakakam, I.; Falath, W.; Kammakakam, I. Nanomaterials: A Review of Synthesis Methods, Properties, Recent Progress, and Challenges. *Mater. Adv.* **2021**, *2*, 1821–1871. [[CrossRef](#)]
3. Roychowdhury, A.; Pati, S.P.; Mishra, A.K.; Kumar, S.; Das, D. Magnetically Addressable Fluorescent Fe₃O₄/ZnO Nanocomposites: Structural, Optical and Magnetization Studies. *J. Phys. Chem. Solids* **2013**, *74*, 811–818. [[CrossRef](#)]
4. Bahari, A.; Roefinard, M.; Ramzannezhad, A.; Khodabakhshi, M.; Mohseni, M. Nanostructured Features and Antimicrobial Properties of Fe₃O₄/ZnO Nanocomposites. *Natl. Acad. Sci. Lett.* **2019**, *42*, 9–12. [[CrossRef](#)]
5. Winatapura, D.S.; Dewi, S.H.; Adi, W.A. Synthesis, Characterization, and Photocatalytic Activity of Fe₃O₄@ZnO Nanocomposite. *Int. J. Technol.* **2016**, *7*, 408–416. [[CrossRef](#)]
6. Feng, Q.; Li, S.; Ma, W.; Fan, H.J.; Wan, X.; Lei, Y.; Chen, Z.; Yang, J.; Qin, B. Synthesis and Characterization of Fe₃O₄/ZnO-GO Nanocomposites with Improved Photocatalytic Degradation Methyl Orange under Visible Light Irradiation. *J. Alloys Compd.* **2018**, *737*, 197–206. [[CrossRef](#)]
7. Liu, K.; Qin, Y.; Muhammad, Y.; Zhu, Y.; Tang, R.; Chen, N.; Shi, H.; Zhang, H.; Tong, Z.; Yu, B. Effect of Fe₃O₄ Content and Microwave Reaction Time on the Properties of Fe₃O₄/ZnO Magnetic Nanoparticles. *J. Alloys Compd.* **2019**, *781*, 790–799. [[CrossRef](#)]
8. Sayadi, M.H.; Sobhani, S.; Shekari, H. Photocatalytic Degradation of Azithromycin Using GO@Fe₃O₄/ZnO/SnO₂ Nanocomposites. *J. Clean. Prod.* **2019**, *232*, 127–136. [[CrossRef](#)]
9. Grecu, R.; Popovici, E.J.; Lădar, M.; Pascu, L.; Indrea, E. Spectroscopic Characterization of Chemical Bath Deposited Cadmium Sulphide Layers. *J. Optoelectron. Adv. Mater.* **2004**, *6*, 127–132.
10. Popa, A.; Toloman, D.; Stan, M.; Stefan, M.; Radu, T.; Vlad, G.; Ulinici, S.; Baisan, G.; Macavei, S.; Barbu-Tudoran, L.; et al. Tailoring the RhB Removal Rate by Modifying the PVDF Membrane Surface through ZnO Particles Deposition. *J. Inorg. Organomet. Polym. Mater.* **2021**, *31*, 1642–1652. [[CrossRef](#)]
11. Pana, O.; Leostean, C.; Soran, M.L.; Stefan, M.; Macavei, S.; Gutoiu, S.; Pop, V.; Chauvet, O. Synthesis and Characterization of Fe-Pt Based Multishell Magnetic Nanoparticles. *J. Alloys Compd.* **2013**, *574*, 477–485. [[CrossRef](#)]
12. Zhu, D.; Zhou, Q. Action and Mechanism of Semiconductor Photocatalysis on Degradation of Organic Pollutants in Water Treatment: A Review. *Environ. Nanotechnol. Monit. Manag.* **2019**, *12*, 100255. [[CrossRef](#)]
13. Ramadan, R.; Ahmed, M.K. Impact of Adding Vanadium Pentoxide to Mn-Doped Magnetite for Technological Uses. *Appl. Phys. A Mater. Sci. Process.* **2022**, *128*, 1056. [[CrossRef](#)]
14. Abbasi, S.; Ahmadpoor, F.; Imani, M.; Ekrami-Kakhki, M.S. Synthesis of Magnetic Fe₃O₄@ZnO@graphene Oxide Nanocomposite for Photodegradation of Organic Dye Pollutant. *Int. J. Environ. Anal. Chem.* **2020**, *100*, 225–240. [[CrossRef](#)]
15. Ammar, S.H.; Abdunabi, W.A.; Kader, H.D.A. Synthesis, Characterization and Environmental Remediation Applications of Polyoxometalates-Based Magnetic Zinc Oxide Nanocomposites (Fe₃O₄@ZnO/PMOs). *Environ. Nanotechnol. Monit. Manag.* **2020**, *13*, 100289. [[CrossRef](#)]
16. Kulkarni, S.D.; Kumbar, S.M.; Menon, S.G.; Choudhari, K.S.; Santhosh, C. Novel Magnetically Separable Fe₃O₄@ZnO Core-Shell Nanocomposite for UV and Visible Light Photocatalysis. *Adv. Sci. Lett.* **2017**, *23*, 1724–1729. [[CrossRef](#)]
17. Zou, P.; Hong, X.; Chu, X.; Li, Y.; Liu, Y. Multifunctional Fe₃O₄/ZnO Nanocomposites with Magnetic and Optical Properties. *J. Nanosci. Nanotechnol.* **2010**, *10*, 1992–1997. [[CrossRef](#)] [[PubMed](#)]
18. Goyal, P.; Chakraborty, S.; Misra, S.K. Multifunctional Fe₃O₄-ZnO Nanocomposites for Environmental Remediation Applications. *Environ. Nanotechnol. Monit. Manag.* **2018**, *10*, 28–35. [[CrossRef](#)]
19. Domínguez-Talamantes, D.; Vargas-Hernández, D.; Hernández-Oloño, J.; Rodríguez-Castellón, E.; Arellano-Cortaza, M.; Castillo, S.; Tánori-Córdova, J. Enhanced photocatalytic activity of FeSO₄ in a ZnO photocatalyst with H₂O₂ for dye degradation. *Optik* **2024**, *304*, 171753. [[CrossRef](#)]
20. Chen, X.; Wu, Z.; Liu, D.; Gao, Z. Preparation of ZnO Photocatalyst for the Efficient and Rapid Photocatalytic Degradation of Azo Dyes. *Nanoscale Res. Lett.* **2017**, *12*, 4–13. [[CrossRef](#)]
21. Pogacean, F.; Ștefan, M.; Toloman, D.; Popa, A.; Leostean, C.; Turza, A.; Coros, M.; Pana, O.; Pruneanu, S. Photocatalytic and Electrocatalytic Properties of NGr-ZnO Hybrid Materials. *Nanomaterials* **2020**, *10*, 1473. [[CrossRef](#)] [[PubMed](#)]
22. Munawar, T.; Alomar, T.S.; Yan, C.; Fatima, S.; Mukhtar, F.; Zakaria, Y.; Iqbal, F. Boosted Charge Separation via Ce₂S₃ over Dual Z-Scheme ZnO-Ce₂S₃-MnO₂ Core Double-Shell Nanocomposite for the Degradation of Diverse Dye Pollutants. *Environ. Res.* **2024**, *251*, 118675. [[CrossRef](#)] [[PubMed](#)]
23. Pana, O.; Petran, A.; Popa, A.; Stefan, M.; Danut, T.; Leostean, C.; Stefan, B.; Pogacean, F.; Toloman, D. Zn_xFe_{3-x}O₄-ZnO Heterojunction Interfaced with Poly (L-DOPA) Electron Transfer Mediator Layer for Enhanced Visible Light Photocatalytic Activity. *J. Alloys Compd.* **2024**, *986*, 174168. [[CrossRef](#)]
24. Jothibas, M.; Manoharan, C.; Johnson Jeyakumar, S.; Praveen, P.; Kartharinal Punithavathy, I.; Prince Richard, J. Synthesis and Enhanced Photocatalytic Property of Ni Doped ZnS Nanoparticles. *Sol. Energy* **2018**, *159*, 434–443. [[CrossRef](#)]
25. Quynh Hoa, N.T.; Lee, Z.; Kim, E.-T. Enhanced Photocatalytic Properties of TiO₂ Nanobelts via In Situ Doping of C and Fe. *J. Electrochem. Soc.* **2011**, *159*, K42–K45. [[CrossRef](#)]

26. Liu, C.; Zhang, L.; Liu, R.; Gao, Z.; Yang, X.; Tu, Z.; Yang, F.; Ye, Z.; Cui, L.; Xu, C.; et al. Hydrothermal Synthesis of N-Doped TiO₂ Nanowires and N-Doped Graphene Heterostructures with Enhanced Photocatalytic Properties. *J. Alloys Compd.* **2016**, *656*, 24–32. [[CrossRef](#)]
27. Yu, J.; Xiang, Q.; Zhou, M. Preparation, Characterization and Visible-Light-Driven Photocatalytic Activity of Fe-Doped Titania Nanorods and First-Principles Study for Electronic Structures. *Appl. Catal. B Environ.* **2009**, *90*, 595–602. [[CrossRef](#)]
28. Alasmari, A.; Alshehri, K.; Azab, A.A.; Solyman, S. Detailed Investigation of the Structural and Electrical Properties of ZnO/Fe₃O₄ Nanocomposites. *Phys. Scr.* **2024**, *99*, 035921. [[CrossRef](#)]
29. Elshypany, R.; Selim, H.; Zakaria, K.; Moustafa, A.H.; Sadeek, S.A.; Sharaa, S.I.; Raynaud, P.; Nada, A.A. Elaboration of Fe₃O₄/ZnO Nanocomposite with Highly Performance Photocatalytic Activity for Degradation Methylene Blue under Visible Light Irradiation. *Environ. Technol. Innov.* **2021**, *23*, 101710. [[CrossRef](#)]
30. Collivignarelli, M.C.; Abbà, A.; Miino, M.C.; Caccamo, F.M.; Torretta, V.; Rada, E.C.; Sorlini, S. Disinfection of Wastewater by Uv-Based Treatment for Reuse in a Circular Economy Perspective. Where Are We At? *Int. J. Environ. Res. Public Health* **2021**, *18*, 77. [[CrossRef](#)]
31. Ferreira, L.C.; Castro-Alferez, M.; Nahim-Granados, S.; Polo-López, M.I.; Lucas, M.S.; Li Puma, G.; Fernández-Ibáñez, P. Inactivation of Water Pathogens with Solar Photo-Activated Persulfate Oxidation. *Chem. Eng. J.* **2020**, *381*, 122275. [[CrossRef](#)]
32. Rahman, Q.I.; Ahmad, M.; Misra, S.K.; Lohani, M. Effective Photocatalytic Degradation of Rhodamine B Dye by ZnO Nanoparticles. *Mater. Lett.* **2013**, *91*, 170–174. [[CrossRef](#)]
33. Al-Gheethi, A.A.; Azhar, Q.M.; Senthil Kumar, P.; Yusuf, A.A.; Al-Buriahi, A.K.; Radin Mohamed, R.M.S.; Al-shaibani, M.M. Sustainable Approaches for Removing Rhodamine B Dye Using Agricultural Waste Adsorbents: A Review. *Chemosphere* **2022**, *287*, 132080. [[CrossRef](#)] [[PubMed](#)]
34. Zheng, Q.; Liu, X.; Tian, L.; Zhou, Y.; Liao, L.; Lv, G. Mechanism of Fenton Catalytic Degradation of Rhodamine B Induced by Microwave. *Chin. Chem. Lett.* **2024**, 109771. [[CrossRef](#)]
35. Wang, J.; Yang, J.; Li, X.; Wang, D.; Wei, B.; Song, H.; Li, X.; Fu, S. Preparation and Photocatalytic Properties of Magnetically Reusable Fe₃O₄@ZnO Core/Shell Nanoparticles. *Phys. E Low-Dimens. Syst. Nanostructures* **2016**, *75*, 66–71. [[CrossRef](#)]
36. Al-Buriahi, A.K.; Al-Gheethi, A.A.; Senthil Kumar, P.; Radin Mohamed, R.M.S.; Yusof, H.; Alsharif, A.F.; Khalifa, N.A. Elimination of Rhodamine B from Textile Wastewater Using Nanoparticle Photocatalysts: A Review for Sustainable Approaches. *Chemosphere* **2022**, *287*, 132162. [[CrossRef](#)] [[PubMed](#)]
37. Rochkind, M.; Pasternak, S.; Paz, Y. Using Dyes for Evaluating Photocatalytic Properties: A Critical Review. *Molecules* **2015**, *20*, 88–110. [[CrossRef](#)] [[PubMed](#)]
38. Pham, H.L.; Hao Nguyen, V.; Vu, T.T.; Khien Nguyen, V.; Ta, N.B.; Le, T.T.; Dang Nguyen, V.; Phung, T.O. Novel 3D Hierarchical Nanostructure of Fe₃O₄/ZnO Hybrid Composites for Enhanced Solar Light Photocatalytic Performance. *J. Mater. Sci. Mater. Electron.* **2021**, *32*, 25018–25032. [[CrossRef](#)]
39. Ahmad, M.; Qureshi, M.T.; Rehman, W.; Alotaibi, N.H.; Gul, A.; Abdel Hameed, R.S.; Al Elaimi, M.; Abd El-Kader, M.F.H.; Nawaz, M.; Ullah, R. Enhanced Photocatalytic Degradation of RhB Dye from Aqueous Solution by Biogenic Catalyst Ag@ZnO. *J. Alloys Compd.* **2022**, *895*, 162636. [[CrossRef](#)]
40. Li, X.; Liu, D.; Song, S.; Zhang, H. Fe₃O₄@SiO₂@TiO₂@Pt Hierarchical Core-Shell Microspheres: Controlled Synthesis, Enhanced Degradation System, and Rapid Magnetic Separation to Recycle. *Cryst. Growth Des.* **2014**, *14*, 5506–5511. [[CrossRef](#)]
41. Williamson, G.K.; Hall, W.H. X-Ray Line Broadening from Filled Aluminium and Wolfram. *Acta Metall.* **1953**, *1*, 22–31. [[CrossRef](#)]
42. Vijayaprasath, G.; Murugan, R.; Palanisamy, S.; Prabhu, N.M.; Mahalingam, T.; Hayakawa, Y.; Ravi, G. Role of Nickel Doping on Structural, Optical, Magnetic Properties and Antibacterial Activity of ZnO Nanoparticles. *Mater. Res. Bull.* **2016**, *76*, 48–61. [[CrossRef](#)]
43. Fatima, H.; Azhar, M.R.; Khiadani, M.; Zhong, Y.; Wang, W.; Su, C.; Shao, Z. Prussian Blue-Conjugated ZnO Nanoparticles for near-Infrared Light-Responsive Photocatalysis. *Mater. Today Energy* **2022**, *23*, 100895. [[CrossRef](#)]
44. Lavorato, G.; Lima, E.; Vasquez Mansilla, M.; Troiani, H.; Zysler, R.; Winkler, E. Bifunctional CoFe₂O₄/ZnO Core/Shell Nanoparticles for Magnetic Fluid Hyperthermia with Controlled Optical Response. *J. Phys. Chem. C* **2018**, *122*, 3047–3057. [[CrossRef](#)]
45. Alyamani, A.A.; Albukhaty, S.; Aloufi, S.; Almalki, F.A.; Al-Karagoly, H.; Sulaiman, G.M. Green Fabrication of Zinc Oxide Nanoparticles Using Phlomis Leaf Extract: Characterization and in Vitro Evaluation of Cytotoxicity and Antibacterial Properties. *Molecules* **2021**, *26*, 6140. [[CrossRef](#)] [[PubMed](#)]
46. El Ghouli, J. Synthesis of Vanadium Doped ZnO Nanoparticles by Sol–Gel Method and Its Characterization. *J. Mater. Sci. Mater. Electron.* **2016**, *27*, 2159–2165. [[CrossRef](#)]
47. Mrabet, S.; Ihzaz, N.; Alshammari, M.; Khlifi, N.; Ba, M.; Bessadok, M.N.; Mejri, I.H.; El Mir, L. Structural, Optical, and Magnetic Properties of V-Doped ZnO Nanoparticles and the Onset of Ferromagnetic Order. *J. Alloys Compd.* **2022**, *920*, 165920. [[CrossRef](#)]
48. Sin, J.C.; Tan, S.Q.; Quek, J.A.; Lam, S.M.; Mohamed, A.R. Facile Fabrication of Hierarchical Porous ZnO/Fe₃O₄ Composites with Enhanced Magnetic, Photocatalytic and Antibacterial Properties. *Mater. Lett.* **2018**, *228*, 207–211. [[CrossRef](#)]
49. Safeen, K.; Safeen, A.; Arif, D.; Shah, W.H.; Ali, A.; Ali, G.; Hussain, F.; Imran, N.; Ullah Shah, A.; Alataway, A.; et al. Tuning the Optical Properties of ZnO by Co and Gd Doping for Water Pollutant Elimination. *Water* **2023**, *15*, 1470. [[CrossRef](#)]
50. Ji, H.; Cai, C.; Zhou, S.; Liu, W. Structure, Photoluminescence, and Magnetic Properties of Co-Doped ZnO Nanoparticles. *J. Mater. Sci. Mater. Electron.* **2018**, *29*, 12917–12926. [[CrossRef](#)]

51. Chiang, Y.D.; Chang, W.Y.; Ho, C.Y.; Chen, C.Y.; Ho, C.H.; Lin, S.J.; Wu, T.B.; He, J.H. Single-ZnO-Nanowire Memory. *IEEE Trans. Electron Devices* **2011**, *58*, 1735–1740. [[CrossRef](#)]
52. Nichols, M.T.; Li, W.; Pei, D.; Antonelli, G.A.; Lin, Q.; Banna, S.; Nishi, Y.; Shohet, J.L. Measurement of Bandgap Energies in Low-k Organosilicates. *J. Appl. Phys.* **2014**, *115*, 094105. [[CrossRef](#)]
53. Li, S.S.; Su, Y.K. Improvement of the Performance in Cr-Doped ZnO Memory Devices: Via Control of Oxygen Defects. *RSC Adv.* **2019**, *9*, 2941–2947. [[CrossRef](#)]
54. Ilyas, U.; Rawat, R.S.; Tan, T.L.; Lee, P.; Chen, R.; Sun, H.D.; Fengji, L.; Zhang, S. Oxygen Rich P-Type ZnO Thin Films Using Wet Chemical Route with Enhanced Carrier Concentration by Temperature-Dependent Tuning of Acceptor Defects. *J. Appl. Phys.* **2011**, *110*, 093522. [[CrossRef](#)]
55. ASLAN, N. Synthesis and Characterization of ZnO@Fe₃O₄ Composite Nanostructures by Using Hydrothermal Synthesis Method. *Türk Doğa Fen Derg.* **2022**, *11*, 95–101. [[CrossRef](#)]
56. Gutiérrez-Pérez, R.M.; Holguin-Momaca, J.T.; Sáenz-Hernández, R.J.; Santillán-Rodríguez, C.R.; Espinosa-Magana, F.; Matutes-Aquino, J.A.; Olive-Méndez, S.F. Sintering Process Effect on the Magnetic Behavior of Vanadium-Doped ZnO Ceramics. *Mater. Res. Express* **2018**, *5*, 036103. [[CrossRef](#)]
57. Yu, W.; Liu, H.; Zhang, L.; Gao, H.; Fu, G. Effect of Intrinsic Vacancies on the Ferromagnetism of V-Doped ZnO Based on First-Principles Calculation. *Phys. Status Solidi Basic Res.* **2010**, *247*, 2185–2189. [[CrossRef](#)]
58. Kayaci, F.; Vempati, S.; Donmez, I.; Biyikli, N.; Uyar, T. Role of Zinc Interstitials and Oxygen Vacancies of ZnO in Photocatalysis: A Bottom-up Approach to Control Defect Density. *Nanoscale* **2014**, *6*, 10224–10234. [[CrossRef](#)]
59. Chankhanittha, T.; Nanan, S. Visible-Light-Driven Photocatalytic Degradation of Ofloxacin (OFL) Antibiotic and Rhodamine B (RhB) Dye by Solvothermally Grown ZnO/Bi₂MoO₆ Heterojunction. *J. Colloid Interface Sci.* **2021**, *582*, 412–427. [[CrossRef](#)]
60. Toloman, D.; Pana, O.; Stefan, M.; Popa, A.; Leostean, C.; Macavei, S.; Silipas, D.; Perhaita, I.; Lazar, M.D.; Barbu-Tudoran, L. Photocatalytic Activity of SnO₂-TiO₂ Composite Nanoparticles Modified with PVP. *J. Colloid Interface Sci.* **2019**, *542*, 296–307. [[CrossRef](#)]
61. Toloman, D.; Popa, A.; Stan, M.; Stefan, M.; Vlad, G.; Ulinici, S.; Baisan, G.; Silipas, T.D.; Macavei, S.; Leostean, C.; et al. Visible-Light-Driven Photocatalytic Degradation of Different Organic Pollutants Using Cu Doped ZnO-MWCNT Nanocomposites. *J. Alloys Compd.* **2021**, *866*, 159010. [[CrossRef](#)]
62. Talukdar, K.; Jun, B.M.; Yoon, Y.; Kim, Y.; Fayyaz, A.; Park, C.M. Novel Z-Scheme Ag₃PO₄/Fe₃O₄-Activated Biochar Photocatalyst with Enhanced Visible-Light Catalytic Performance toward Degradation of Bisphenol A. *J. Hazard. Mater.* **2020**, *398*, 123025. [[CrossRef](#)] [[PubMed](#)]

Disclaimer/Publisher’s Note: The statements, opinions and data contained in all publications are solely those of the individual author(s) and contributor(s) and not of MDPI and/or the editor(s). MDPI and/or the editor(s) disclaim responsibility for any injury to people or property resulting from any ideas, methods, instructions or products referred to in the content.